Ultrasound Pixel-Based Beamforming With Phase Alignments of Focused Beams

Nghia Q. Nguyen and Richard W. Prager

Abstract—We previously developed *unified pixel-based (PB) beamforming* to generate high-resolution sonograms, based on field pattern analysis. In this framework, we found that the transmit waveshape away from the focus could be characterized by two spherical pulses. These correspond to the maximal and minimal distances from the imaging point to the active aperture. The beamformer uses this model to select the highest energy signals from backscattered data. A spatiotemporal interpolation formula is used to provide a smooth transition in regions near the focal depth where there is no dominant reflected pulse. In this paper, we show that the unified PB approach is less robust at lower center frequencies. The interpolated data is suboptimal for a longer transmit waveshape. As a result, the spatial resolution at the focal depth is lower than that in other regions. By further exploring the field pattern, we propose a beamformer that is more robust to variations in beamwidth. The new method, named *coherent PB beamforming*, aligns and compounds the pulse data directly in the transition regions. In simulation and phantom studies, the coherent PB approach is shown to outperform the unified PB approach in spatial resolution. It helps regain optimal resolution at the focal depth while still maintaining good image quality in other regions. We also demonstrate the new method on *in vivo* data where its improvements over the unified PB method are demonstrated on scanned objects with a more complicated structure.

Index Terms—Coherent beamforming, image quality, pixel-based (PB) beamforming, spatial resolution, ultrasound, virtual source.

I. INTRODUCTION

PIXEL-BASED (PB) beamforming has been developed recently as a way to generate B-mode images with improved resolution. It avoids interpolation artifacts by performing dynamic focusing individually for every point in the image [1], [2]. Similar to *synthetic aperture* (SA) imaging [3], [4], a high-resolution image can be formed by compounding the low-resolution images created from individual pulse-echo sequences. Unlike SA imaging that involves the use of defocused pulses, however, PB beamforming is based on a conventional focused ultrasonic transmission. Because the beam is narrower, data superposition is usually limited to a small number of transmit–receive cycles. In its simplest form, PB beamforming generates data at each imaging point using only signals backscattered from the nearest transmit event [1], [5].

Attempts to extend the superposition to include transmission events further across the active aperture lead to the use of the

virtual source element (VSE) technique [6]. In this approach, a source is assumed to exist at the transmit focus and a spherical wave is considered to propagate back and forth from this point [7], [8]. Zemp and Insana [9] showed that the VSE approach can achieve spatial resolution in the near and far fields similar to that at the focal depth. The spherical waveshape, however, is only a good approximation within a limited angle. Outside this angle, the wave shape assumption is invalid. The VSE approach therefore requires that we discard these data, which could otherwise benefit the image reconstruction [6], [10]. The lack of a way to incorporate these data may create errors in the B-mode image especially when there is high echogenicity around the focal depth. Such errors can be avoided by setting the focal length outside the imaging region [11]. This strategy, however, broadens the transmit beam and compromises the spatial resolution.

In [12], we developed a unified PB beamformer that is implemented with a highly focused transmit beam. Our motivation was to demonstrate high-resolution reconstruction at all image depths using a conventional focused transmit–receive acquisition sequence. Through field pattern analysis, we modeled the transmitted waveshape at points away from the focus as two weak pulses. The arrival times of these pulses correspond to the maximal and minimal distances from the imaged point to the active aperture. This leads to a generalization of the VSE technique that is valid over the entire imaging region. Based on this finding, we developed an algorithm to compute the appropriate time delay for each received signal in the beamformer. It combines the VSE technique to extract data associated with the highest energy received pulse and a heuristic interpolation formula to give a smooth transition in regions where the VSE technique is not applicable. The unified PB beamformer was shown to generate high-resolution images when applied to both experimental and *in vivo* data.

In [13], however, we found that the unified PB was less robust when applied to data acquired with a lower center frequency. As the transmit beam becomes broader, the unified PB requires more data from the heuristic interpolation formula to generate a smooth transition around the focal depth. This degrades the image resolution at the focal depth because the heuristic formula is suboptimal for selecting focused signals in the transition between the two pulses. This is in contrast to the performance of many conventional algorithms where the image has best resolution at the focal depth. It motivates us to investigate the field pattern further, update the unified PB beamformer, and develop a new method that is more robust to variations in the center frequency.
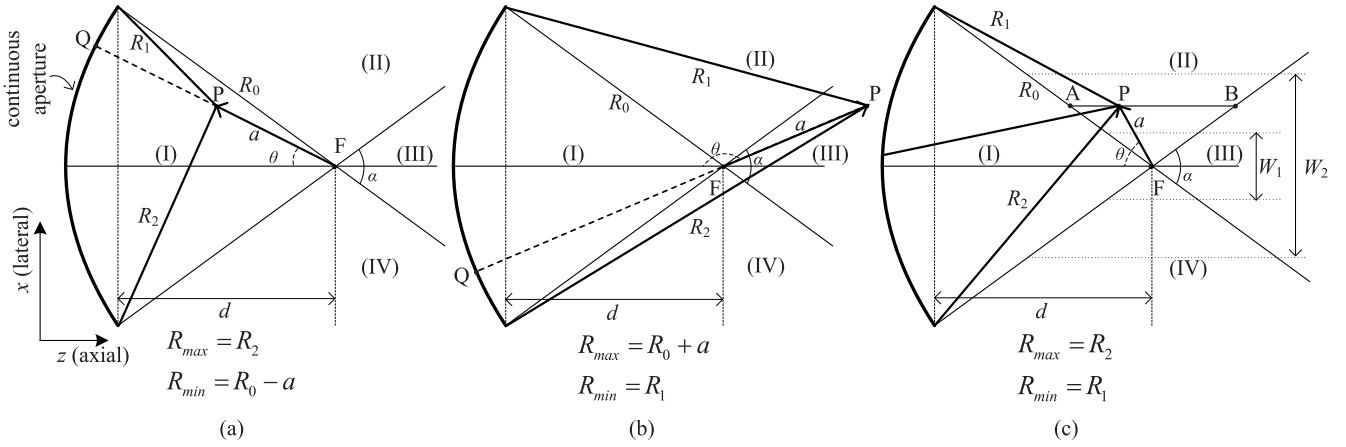
Fig. 1. Geometries for field profile analysis and time delay calculations with a transmit beam. The transmit delays associated with the elements of the active linear aperture are represented by the curvature of the aperture in the axial–lateral plane (from [12, Fig. 1]). Angle α at the transmit focus F divides the plane into four regions, denoted from (I) to (IV) clockwise. The figure plots different scenarios for an imaging point P, including (a) P in region (I), (b) P in region (III), and (c) P in region (II). The imaging point in region (IV) is treated the same as that in region (II). The same notation is used in (a)–(c).

This paper is organized as follows. In Section II, we briefly summarize the field pattern profile and the unified PB beamformer developed in [12]. We then present a new method, named *coherent PB beamforming*, based on an extension of this analysis. In Section III, we demonstrate the new method and compare it to the unified PB beamformer using simulations [14], [15] and experimental data acquired with an instrumented ultrasound machine [16]. Beamformer performance is evaluated qualitatively and quantitatively based on the generated images. We also demonstrate the coherent PB beamformer on *in vivo* data from an ultrasound scan of the carotid artery. The imaging results verify the robustness of the new method to structural complexity of the scanned object in clinical applications. Finally, we summarize and draw some conclusions in Section IV.

II. METHODS

A. Pixel-Based Beamforming

Similarly to SA imaging [4], PB beamforming uses time delay information to align and assemble signals received at individual elements for each image point P. The beamformed signal is generated by

$$g(\mathbf{x}_p) = \sum_{i}^{N_t} \sum_{j}^{N_r} w_{i,j} r_{i,j}(\tau_p(i,j)) \tag{1}$$

where N_t is the number of transmits, N_r is the number of receiving elements in the active aperture, $r_{i,j}(t)$ is the waveform or echo RF trace received on element j with transmit i, the $w_{i,j}$'s are apodization coefficients, and $\tau_p(i,j)$ is the time delay used to extract signals from the received waveform $r_{i,j}(t)$.

The receive time delay (between backscatter and reception at the probe) is calculated straightforwardly based on the distance between P and the corresponding receiving element (given the sound speed c is known). Thus, beamformer performance depends on appropriate calculation of the transmit time delays from the probe excitation to the intended target P. Conventionally, this delay is calculated by assuming the transmit pulse is spherical and propagates from the center of the active aperture [2], [3]. This assumption, however, only holds within a limited angular extent for each transmit [4]. Far from the transmit centerline, the conventional time delay results in adding noise and off-target interference to the beamformed image, rather than the echo from the intended target. This limits the image from being generated with a large number of transmits.

In this paper, we have analyzed the pressure field to develop a better time delay calculation. The analysis is based on a combination of the *impulse response* method [17] and simulation using the Field II program [14], [15]. In the following section, we briefly summarize our earlier work that lays the foundation for the unified PB beamforming in [12]. We then further extend it to develop the new PB beamformer, which is the focus of this paper.

B. Extended Field Pattern Analysis

We take the transmit delay at individual elements into account and model the aperture as a continuous uniform arc with a focal depth d and radius R_0 [9]. From the focal point F, we divide the imaging plane into four regions using the limited angle α in the virtual source approach [7], [8]. The regions, denoted from (I) to (IV) clockwise, are shown in Fig. 1(a)–(c) with different scenarios for the image point P with respect to the aperture. A point in region (IV) will have the same treatment as one in region (II), and thus it is not shown in Fig. 1.

In the analysis, we use four geometrical distances to characterize the transmit waveshape. These are $R_{\max}$ and $R_{\min}$, which are the maximal and minimal distances from P to the aperture, and R_1 and R_2 from P to the edges of the aperture. For P in region (I) [Fig. 1(a)], the pressure field is given by

$$p(\mathbf{x}_p, t) = \frac{\rho c \beta_q}{\pi} v\left(t - \frac{R_{\min}}{c}\right)$$
$$- \frac{\rho c}{2\pi}\left[\beta_1 v\left(t - \frac{R_1}{c}\right) + \beta_2 v\left(t - \frac{R_2}{c}\right)\right] \tag{2}$$

where $v(t)$ is the excitation, ρ is the equilibrium density of the medium, and β_1, β_2, and β_q are the angular coefficients
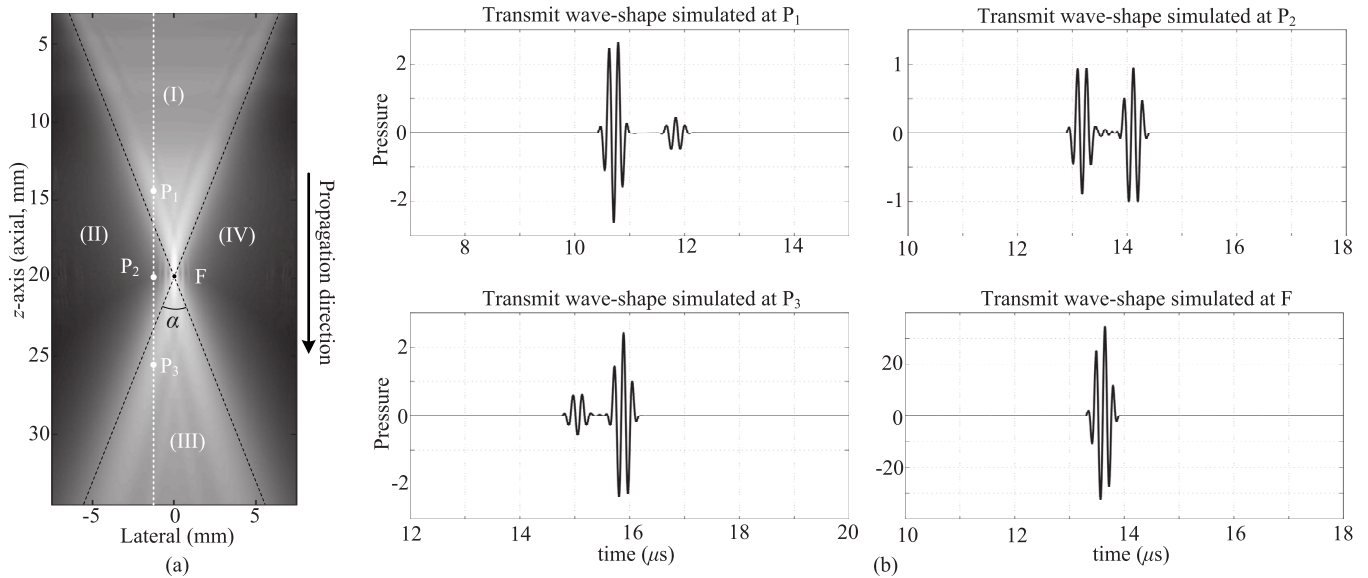
Fig. 2. (a) Pattern field from one transmit event simulated after the ULA-OP system and transducer LA523 using the Field II program. (b) Transmit waveshapes generated at imaging points P_1, P_2, and P_3, and the focus F. All waveshapes are normalized to the amplitude of that simulated at P_2.

associated to R_1, R_2, and R_{min} (derived from point Q on the aperture), respectively. Depending on the position of P inside region (I), the maximal distance R_{max} is either R_1 or R_2. The waveshape has three pulses; however, it is dominated by the highest energy pulse associated with R_{min}.

For P in region (III) [Fig. 1(b)], we have the pressure field

$$p(\mathbf{x}_p, t) = \frac{\rho c}{2\pi}\left[\beta_1 v\left(t - \frac{R_1}{c}\right) + \beta_2 v\left(t - \frac{R_2}{c}\right)\right] - \frac{\rho c \beta_q}{\pi} v\left(t - \frac{R_{max}}{c}\right) \qquad (3)$$

where β_q is the angular coefficient associated with R_{max}. In this region, the transmit waveshape has three pulses but is dominated by the one associated with R_{max}. Also depending on the position of P, the pulse with either R_1 or R_2 corresponds to the minimal distance R_{min}.

For P in region (II) [Fig. 1(c)]

$$p(\mathbf{x}_p, t) = \frac{\rho c}{2\pi}\left[\beta_1 v\left(t - \frac{R_1}{c}\right) - \beta_2 v\left(t - \frac{R_2}{c}\right)\right]. \qquad (4)$$

These two pulses are associated with R_1 and R_2. In this case, R_1 and R_2 are actually R_{min} and R_{max}, respectively. The pressure field contains only two pulses and neither of them consistently dominates the waveshape. The first pulse, associated with R_1, has a higher magnitude near region (I), while the second pulse, associated with R_2, becomes larger near region (III).

At the focal point F, all R_{max}, R_{min}, R_1, and R_2 are the same and the pulses are merged into one highly focused pulse. At other positions, however, the excitation pulses at transmit elements are out-of-phase. The waveshape is separated into several *out-of-focus pulses*. Based on the analysis, we approximate the waveshape as a combination of the two pulses corresponding to the distances R_{max} and R_{min} from P to the active aperture. We denote them by the *min pulse* and *max pulse* and use the information of their arrival times to form the transmit time delay calculation.

This analysis also reveals the relationship between the phases of the max and min (distance) pulses in the transmit waveshape. For P in region (I), the min pulse corresponds to R_{min}, while the max is one of those associated with R_1 or R_2. From (2), we can see that in either case, the max pulse is phase inverted with respect to R_{min}. Similarly for P in region (III) where the waveshape is generated in (3), the min pulse corresponds to either R_1 or R_2, and in both cases are phase inverted with respect to the R_{max} pulse. Furthermore, it is clear from (4) that the two pulses are phase inverted with respect to each other for P in region (II).

We confirm these new findings relating to phase inversion using Field II simulations. First, we generate the field pattern of the transmit beam, modeled after the ultrasound advanced open platform (ULA-OP) system described in Section III, and show it in Fig. 2(a). In Fig. 2(b), we plot the simulated transmit waveshapes at four imaging points P_1, P_2, P_3, and the transmit focus F. The positions of these points are shown in Fig. 2(a). In Fig. 2(a), the waveshape at F includes only one pulse with the highest magnitude. At other points, the pulse is broken into two much weaker pulses, almost completely out-of-phase with each other.

Our analysis has some limitations. Besides the approximation from a discrete linear array to a continuous uniform arc, we ignore the directivity of transducer elements by assuming each of them to be a point source. The analysis also does not include the effects of diffractions near the transducer surface. In the study, however, we are not trying to develop a comprehensive study on the field patterns. Our goal is to extract important information about the transmit beam that can be used to enhance beamformer performance.

C. Unified Pixel-Based Beamformer [12]

The unified PB approach generates focusing data with a time delay calculation based on the arrival times of the min and max pulses. As our study focuses on the transmit time

delay in a pulse-echo sequence, we drop indices i and j in $\tau_p(i, j)$ of (1) and use τ_p to denote the transmit time delay to point P.

The selection is obvious in region (I) or (III) where the waveshape is dominated by the min or max pulse, respectively. The time delay for P in region (I) is given by

$$\tau_p = \tau_{p,\min} = \frac{d - a}{c} \qquad (5)$$

and for P in region (III), it is given by

$$\tau_p = \tau_{p,\max} = \frac{d + a}{c}. \qquad (6)$$

These calculations include the delay $\tau_0 = (R_0 - d)/c$ so that the total delay is given with reference to the time at which the last (or central) element fires [12].

In region (II) or (IV), the selection of the dominant pulse is more difficult because the max and min pulses have similar magnitudes. For an artifact-free reconstruction, it is important to have a smooth travel time field over the whole imaging region. An abrupt change in this field causes artifacts at the corresponding locations in the image. The smooth transition from $\tau_{p,\min}$ in region (I) to $\tau_{p,\max}$ in region (III), however, happens only at the focus F. Thus, in [12], we proposed a method to calculate τ_p for P in region (II) [and the same for region (IV)] as

$$\tau_p = \frac{|\mathbf{x}_b - \mathbf{x}_p|}{|\mathbf{x}_b - \mathbf{x}_a|}\tau_{p,1} + \frac{|\mathbf{x}_a - \mathbf{x}_p|}{|\mathbf{x}_a - \mathbf{x}_b|}\tau_{p,2} \qquad (7)$$

where $\mathbf{x}_a$, $\mathbf{x}_b$, and $\mathbf{x}_p$ are vector positions of points A, B, and P [see Fig. 1(c)]. We assume that the origin of these vectors is at the center of the active aperture. The time delays $\tau_{p,1}$ and $\tau_{p,2}$ are given by

$$\tau_{p,1} = \frac{R_1}{c} - \tau_0 \quad \text{and} \quad \tau_{p,2} = \frac{R_2}{c} - \tau_0. \qquad (8)$$

As $\tau_{p,1} = \tau_{p,\min}$ when P is at A and $\tau_{p,2} = \tau_{p,\max}$ when P is at B, this calculation provides a linear transition from $\tau_{p,\min}$ to $\tau_{p,\max}$. The time delay calculation in (5)–(7) is a combination comprising the VSE technique plus a linear transition between the highest energy pulses when P is outside the limited angle.

The imaging data collected at P in regions (II) and (IV) are important for generating an artifact-free image. For P that are deep in those regions and far from the beam centerline, however, the transmit pulses are weak. The τ_p in (7) increasingly refers to an even weaker signal between these two pulses. The selected echo data, therefore, is dominated by backscattered noise and off-target interference and contributes very little information to the reconstructed image. Thus, we use the apodization coefficients $w_{i,j}$ to regularize the signals and limit the noise added into the beamformer calculation.

Specifically, we set $w_{i,j}$ equal to 1 for P in regions (I) or (III). For P in region (II) or (IV), we set $w_{i,j}$ equal to 1 within an interval W_1 and 0 outside an interval W_2 [see Fig. 1(c)]. Between these areas, $w_{i,j}$ is set by linearly reducing from 1 to 0. Parameters W_1 and W_2 are selected based on *ad hoc* methods as well as the visualization and comparison of generated images. Through experiments

with various center frequencies, we find that the unified PB beamformer can produce an image with good quality using $W_1 \approx \lambda f_0/D$ and $W_2 \approx 3\lambda f_0/D$, where λ is the wavelength, f_0 is the focal depth, and D is the width of the transmit aperture. The term $\lambda f_0/D$ is the azimuthal resolution of the transmit beam [17].

D. Coherent Pixel-Based Beamformer

In an attempt to incorporate more data from regions (II) and (IV), we propose a new method that directly selects signals associated with the two pulses in the transmit waveshape. First, we modify the imaging equation in (1) to become

$$g(\mathbf{x}_p) = \sum_i^{N_t} \sum_j^{N_r} w_{i,j}\, y_p(i, j) \qquad (9)$$

where $y_p(i, j)$ is synthesized from the data in the received waveform $r_{i,j}(t)$. A major difference of the new method from the unified PB beamformer is that $y_p(i, j)$ can be integrated from more than one data point in $r_{i,j}(t)$. In particular, it combines the high energy signals associated with the max and min pulses in the transmit waveshape at individual imaging points. In order to be of value, this combination will need to take into account the phase inversion between these two pulses.

For P in region (I), we choose $y_p(i, j) = r_{i,j}^{\min}$, which is the data point on $r_{i,j}(t)$ associated with $\tau_{p,\min}$. For P in region (III), we choose $y_p(i, j) = -r_{i,j}^{\max}$, which is the data associated with $\tau_{p,\max}$. This is still the same as for the unified PB beamformer except for the inclusion of a "$-$" sign for phase inversion in region (III).

In region (II) [or region (IV)], we calculate $y_p(i, j)$ as

$$y_p(i, j) = \frac{|\mathbf{x}_b - \mathbf{x}_p|}{|\mathbf{x}_b - \mathbf{x}_a|}r_{i,j}^1 - \frac{|\mathbf{x}_a - \mathbf{x}_p|}{|\mathbf{x}_a - \mathbf{x}_b|}r_{i,j}^2 \qquad (10)$$

where $r_{i,j}^1$ and $r_{i,j}^2$ are extracted from $r_{i,j}(t)$ with time delays $\tau_{p,1}$ and $\tau_{p,2}$, respectively. As $r_{i,j}^1 = r_{i,j}^{\min}$ for P at A and $r_{i,j}^2 = r_{i,j}^{\max}$ for P at B, this scheme also provides a smooth transition from the min to the max pulse when P is outside the limited angle. Note the "$-$" sign again to account for the phase inversion.

The new method aligns data associated with the max and min pulses propagating to the image point P from different transmits and combines them, with phase alignment, to generate an artifact-free image. The appropriately delayed and summed waveforms increase the net echo coherence, which improve the lateral resolution of the generated image. We call this approach the *coherent PB beamformer*.

In this coherent PB approach, we also use a similar apodization scheme based on W_1 and W_2 [see Fig. 1(c)] to prevent noise from out-of-focus regions contributing to the image generation process. Because we now have valid data over a greater area, we can set W_1 and W_2 wider than those for the unified PB. Specifically, $W_1 \approx 4\lambda f_0/D$ and $W_2 \approx 8\lambda f_0/D$, where $\lambda f_0/D$ is the azimuthal resolution of the transmit beam.

III. Results and Discussion

A. Data Acquisition and Processing

In this section, we demonstrate and compare the performance of the coherent PB with other beamformers. They are applied to data acquired with the ULA-OP ultrasound system [16]. The transducer is a linear array of 192 elements (LA523, Esaote SpA, Florence, Italy) with 64 elements active in each transmit event. The transmit beam is focused at 20 mm. In elevation, the aperture is weakly focused also at 20 mm using an acoustic lens. The beam is generated with a center frequency f_0 of 6.0 MHz and a 40% pulse-echo bandwidth. It is stepped by an element pitch of 0.245 mm laterally. Received waveforms are sampled at 50 Msamples/s, resulting in an axial sampling interval of 0.0154 mm. In each pulse-echo sequence, the transmit beam is shifted laterally by a step of one element pitch. The dynamic focused image, therefore, is generated with a 0.245-mm sampling interval in the lateral direction. The PB beamformers improve image quality by generating RF data at points between the scanlines. We choose to generate the PB images with a fivefold finer grid in the lateral direction, which results in a 0.049-mm sampling interval.

B. Evaluation Metrics

We evaluate each beamformer through the quality of the generated B-mode images, measured with three metrics: spatial resolution, contrast ratio, and echo signal-to-noise (eSNR) [18]. The spatial resolution is quantified by measuring the width of simulated point target responses. In phantom studies, we evaluate the spatial resolution through the speckle size or coherence length of the generated images [19], [20], given by

$$S_c = \int_{-\infty}^{\infty} \frac{C_X(\mathbf{x})}{C_X(0)} d\mathbf{x} \tag{11}$$

where $C_X(\mathbf{x})$ is the spatial autocovariance function for the RF data and $d\mathbf{x}$ is the sampling interval 2-D vector. As the PB beamformers only have an impact on the lateral resolution, we measure this metric, denoted by S_{cx}, in the lateral direction only.

The eSNR is calculated using the ratio of the ensemble energy of the beamformed echo signals over the noise power. We calculate the echo energy and noise using average/difference over 12 beamformed RF frames acquired in the same scan location. The calculation is performed using kernels that contain no strong reflectors to avoid the effects of sidelobes on the noise power [18].

The contrast ratio (CR) between a lesion and the background is quantified by [21]

$$CR = \frac{I_{out} - I_{in}}{\sqrt{I_{out}^2 + I_{in}^2}} \tag{12}$$

where I_{in} and I_{out} are the mean intensities (in decibels) measured inside and outside the lesion, respectively. The term CR has a value of 1 for perfect contrast and a value of 0 for no contrast between the lesion and background.
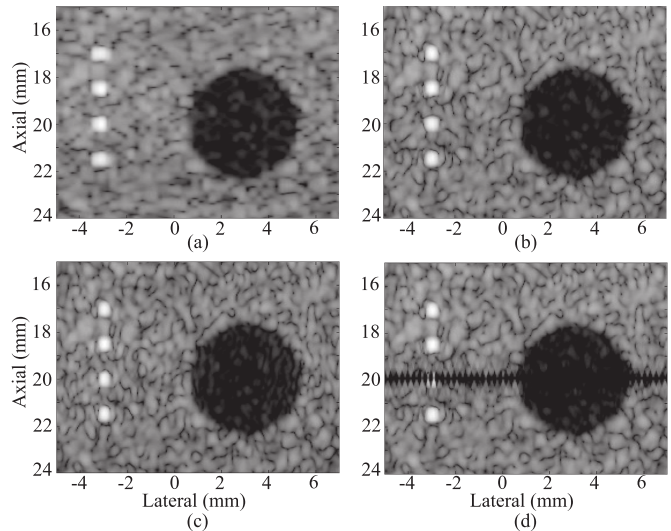

Fig. 3. Simulated images of a phantom that contains four point scatterers and an anechoic cyst suspended in a random background. The scatterers are located at -3 mm laterally and at 17, 18.5, 20, and 21.5 mm in depth, while the cyst is 5 mm in diameter and centered at $(z, x) = (20, 3)$ mm. The images are generated with different strategies. (a) Conventional dynamic focusing, (b) unified PB beamformer, (c) coherent PB beamformer, and (d) VSE technique, where imaging data outside the limited angle are discarded. Images in (b)–(d) are generated with data from 32 transmits. All images are log-compressed and displayed with a dynamic range of 60 dB.

The background kernel is selected to have the same area as the lesion. To minimize the effect of variations in the attenuation and diffraction of the ultrasound, we choose the kernel as a circular ring enclosing the lesion.

C. Simulation

The simulated data are generated with the Field II program configured to model the ULA-OP system described above. The numerical phantom has a random background with four scatterers suspended at depths from 17 to 21.5 mm with a 1.5-mm separation. The scatterers line up at -3 mm in the lateral direction. There is also an anechoic cyst, 5 mm in diameter centered at $(z, x) = (20, 3)$ mm. The scatterers' strength inside the cyst is 20 times less than the strength of those in the background, equivalent to -26 dB relative to the root-mean-square amplitude of the background signal. The simulated data contain no noise, and thus we evaluate the images using just the spatial resolution and contrast ratio.

Imaging results generated with different beamformers are shown in Fig. 3. The dynamic focused image shown in Fig. 3(a) is interpolated to have the same pixel size as the PB beamformed images. Compared with those generated with the unified and coherent PB in Fig. 3(b) and (c), we find the resolution is much improved and blurring artifacts caused by interpolation are removed. To show the advantages of integrating data in out-of-focus regions, we apply the VSE calculation to the prebeamformed signals. In this calculation, we follow suggestions in [6] and [10] to discard the data outside the limited angle [regions (II) and (IV) in our analysis]. The result is shown in Fig. 3(d) with errors at the focal depth. These errors result from not including all imaging data that are
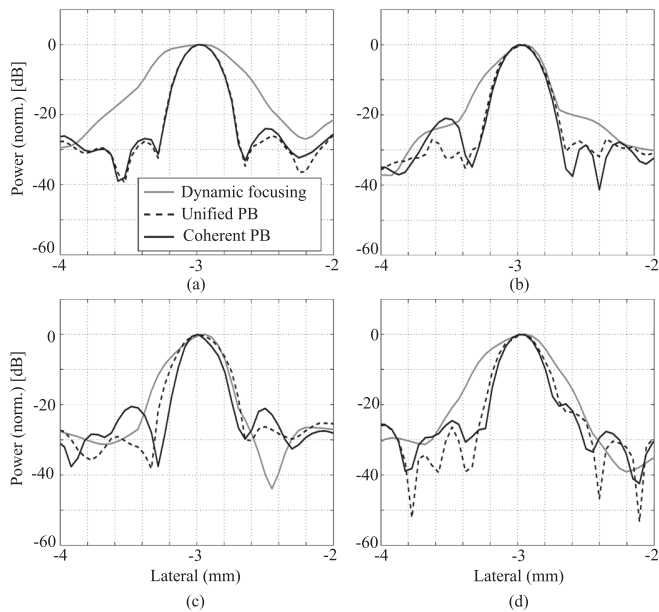
Fig. 4.   Lateral profiles of scatterers at depths of (a) 17, (b) 18.5, (c) 20, and (d) 21.5 mm. The legend in (a) also applies to (b)–(d).

TABLE I
COMPARISON BETWEEN THE UNIFIED PB AND COHERENT
PB BEAMFORMERS THROUGH FWHMs OF THE
POINT TARGET RESPONSES

Beamformer	FWHM at a depth of			
	17 mm	18.5 mm	20 mm	21.5 mm
Dynamic focusing	0.626 mm	0.368 mm	0.367 mm	0.478 mm
Unified PB	0.305 mm	0.308 mm	0.346 mm	0.318 mm
Coherent PB	0.299 mm	0.292 mm	0.263 mm	0.280 mm

relevant around the focal depth. It is shown in Fig. 3(d) that these errors cannot be corrected using time gain compensation alone.

To enable a more detailed comparison, we plot the lateral beamformer profiles of these scatterers in Fig. 4. The responses are not symmetric on these plots because the point scatterers are suspended against a random background. Compared with the unified PB, the coherent PB shows narrower mainlobes at all depths. This indicates the better resolution generated by the coherent PB. The greatest improvement is observed at 20 mm; this is the depth with the smallest mainlobe for the coherent PB but is also the worst performing depth for the unified PB. Thus, the coherent PB is able to recover optimal resolution at the focal depth of the generated images. At this depth, dynamic focusing has a mainlobe width closest to those of other beamformers. This indicates that it achieves its optimal resolution around this region. At other depths, it generates beam profiles with much broader mainlobes. The beamwidths at −6 dB are measured and summarized in Table I.

Both unified and coherent PB show improvements over the dynamic focused image in the CR of the simulated anechoic cyst. For dynamic focusing, CR = 0.803, while those measured on the unified and coherent PB images are 0.866 and 0.843, respectively. To enable a more detailed
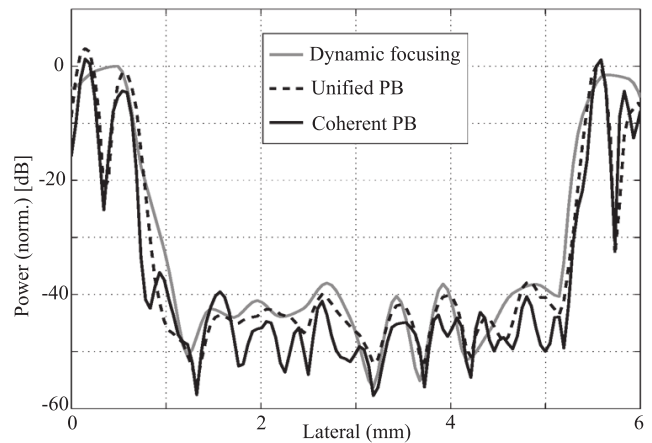
comparison, we plot in Fig. 5 a lateral section through the cyst for each image at a depth of 20 mm. In Fig. 5, the coherent PB shows individual scatterer features with a sharper profile indicating the higher spatial resolution. Meanwhile, the dynamic focused image has a smooth curve caused by the blurring interpolation artifacts.

Fig. 5.   Lateral section through the anechoic cyst using each of the algorithms at a depth of 20 mm.

D. Phantom Study

Experimental data are acquired by scanning a tissue-mimicking phantom (manufactured by the Department of Medical Physics, University of Wisconsin, Madison, WI, USA). The manufacturer reported speeds of sound ranging from 1538 to 1551 m/s and an attenuation coefficient slope of 0.55 dB·cm^{-1}·MHz^{-1}.

The first experimental scan includes two hyperechoic circular targets, 5 mm in diameter, positioned around the depths of 9 and 23.5 mm. The dynamic focused envelope is interpolated and displayed in Fig. 6(a). The images from the unified and coherent PB beamformers are shown in Fig. 6(b) and (c), respectively. The imaging results show the strengths and limitations of the unified PB beamformer. Although it offers much higher spatial resolution than conventional dynamic focusing, the speckles at the focal depth are wider than those in the far field. Meanwhile, the coherent PB approach offers the finest speckle pattern at the focal depth. This improvement comes from the data selection associated with the max and min pulses in the out-of-focus regions. This, in turn, allows a larger amount of high-energy data to be combined in the beamforming summation. In the near-field and far-field regions, most of the data are extracted using either the min or max pulse alone, in both coherent and unified PB beamfomers. Hence, the speckle patterns in these regions look the same in both images.

To demonstrate the advantages of the coherent PB more clearly, we generated another unified PB image using the same apodization applied to the coherent PB. Hence, the windows W_1 and W_2, used to specify the apodization for the unified PB [see Fig. 1(c)], are enlarged to approximately four and eight times of the azimuthal resolution. The generated unified
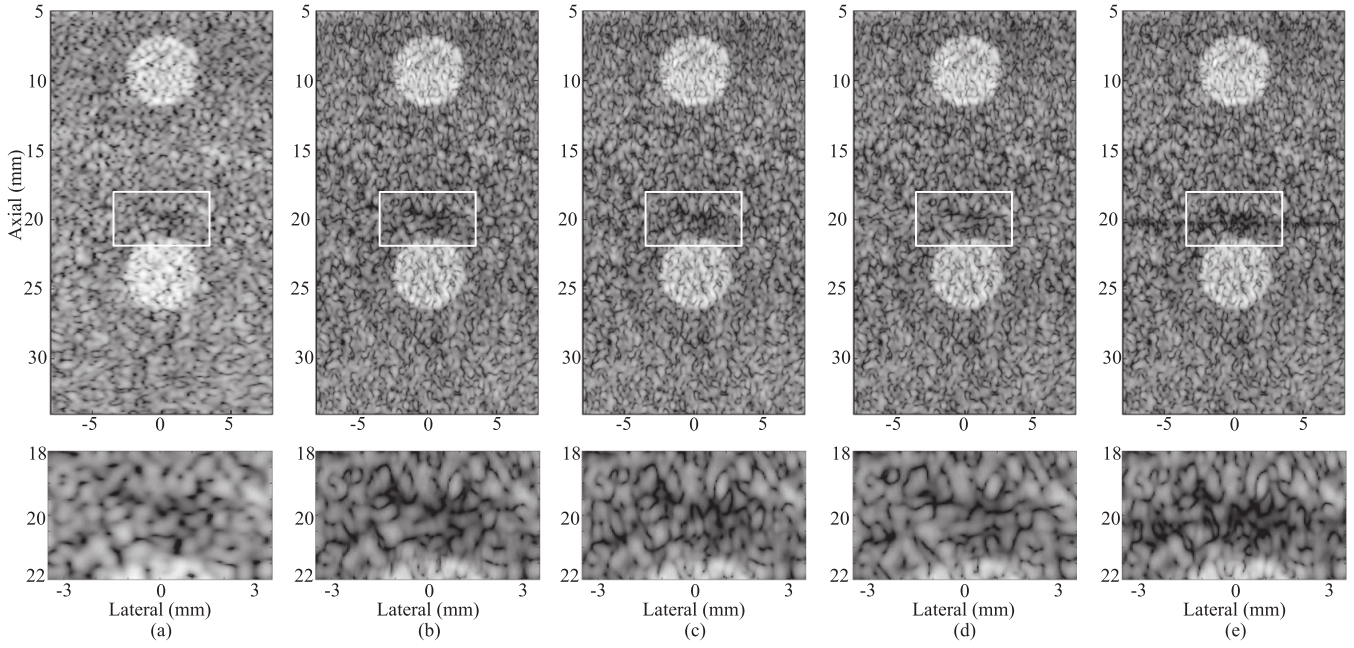
Fig. 6. Top: images of two idealized hyperechoic lesions generated with different beamforming strategies. (a) Conventional dynamic focusing, (b) unified PB, (c) coherent PB, (d) unified PB with the same apodization coefficient as the coherent PB, and (e) coherent PB, where data are combined without phase inversion. The data are acquired with a center frequency of 6.0 MHz. (b)–(e) Images are generated with data from 32 transmits. Bottom: regions enclosed by the white rectangles in (a)–(e) are magnified for detailed comparison. All images are log-compressed and displayed with a dynamic range of 45 dB.

TABLE II
PERFORMANCE METRICS MEASURED ON EXPERIMENTAL
DATA OF A 6-MHz CENTER FREQUENCY

Beamformers	S_{cx} (focal, mm)	S_{cx} (far-field, mm)	eSNR (dB)
Dynamic focusing	0.53±0.02	0.74±0.05	36.39±3.11
Unified PB	0.43±0.01	0.37±0.01	39.06±4.09
Coherent PB	0.36±0.01	0.37±0.01	38.74±3.60
Unified PB (with wider $W_{1,2}$)	0.44±0.02	0.37±0.01	37.32±3.41

Azimuthal resolution $\lambda f^\sharp = 0.332$ mm.

TABLE III
PERFORMANCE METRICS MEASURED ON EXPERIMENTAL
DATA OF A 3.5-MHz CENTER FREQUENCY

Beamformers	S_{cx} (focal, mm)	S_{cx} (far-field, mm)	eSNR (dB)
Dynamic focusing	0.77±0.02	1.45±0.05	33.63±0.51
Unified PB	0.74±0.02	0.70±0.02	37.09±0.27
Coherent PB	0.62±0.01	0.70±0.02	36.55±0.22
Unified PB (with wider $W_{1,2}$)	0.73±0.02	0.70±0.02	34.75±0.11

Azimuthal resolution $\lambda f^\sharp = 0.57$ mm.

PB image with the matched apodization is displayed in Fig. 6(d). The speckle patterns look almost the same as those shown in Fig. 6(b), indicating no gain in spatial resolution. We also demonstrate the impact of the phase inversion used in the coherent PB by generating another coherent PB image without it. The result is shown in Fig. 6(e). In the new coherent PB image, there is a horizontal line across at the focal depth indicating the loss of coherence in the reconstruction.

For each image, we measure the speckle size and eSNR and summarized the results in Table II. In the near field, the pressure field contains *a quadratic phase factor* [22] that causes fluctuations in the wavefront. As a result, the speckle granularity is not a valid indication of resolution and the correlation-based metric may not provide an accurate evaluation. We therefore measure the speckle sizes in the far field and in the focal region, where the effects caused by the quadratic phase factor are much less. The eSNR is calculated on homogenous regions from 16 to 24 mm, at the two sides of

the lesion to avoid effects from strong reflectors. In Table II, it shows that the unified PB image generated with the matched apodization to the coherent PB (unified PB with wider $W_{1,2}$) has the lowest eSNR. This indicates the advantage of selecting focused signals in the coherent PB approach. Furthermore, using wider apodization in the unified PB, we lower the eSNR of the generated image for no gain in the spatial resolution.

To further illustrate the improvements of the coherent PB, we demonstrate the beamformers on a second experimental data set. Imaging data are acquired using the same transducer and system parameters but with the center frequency reduced to 3.5 MHz. The scan contains an anechoic lesion, 5 mm in diameter, positioned at 23.5 mm. Images generated with different beamformers are shown in Fig. 7(a)–(d). They are, respectively, for the dynamic focusing, unified and coherent PB, and unified PB beamformers with apodization matched to the coherent PB. Fig. 7(c) shows that the speckle pattern is the finest at the focal depth in the coherent PB images.
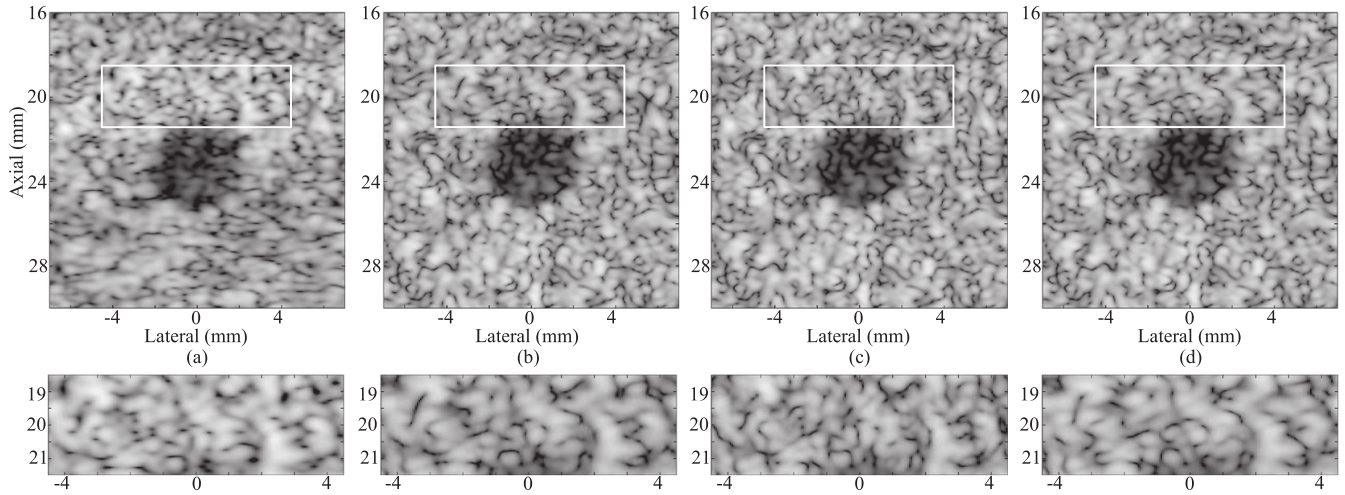
Fig. 7. Top: images of an idealized anechoic lesion generated with (a) conventional dynamic focusing, (b) unified PB beamformer, (c) coherent PB beamformer, and (d) unified PB beamformer with the same apodization coefficient as the coherent PB beamformer. The data are acquired with a center frequency of 3.5 MHz. (b)–(d) Images are generated with data from 32 transmits. Bottom: regions enclosed by the white rectangles in (a)–(d) are magnified for a detailed comparison. All images are log-compressed and displayed with a dynamic range of 40 dB.
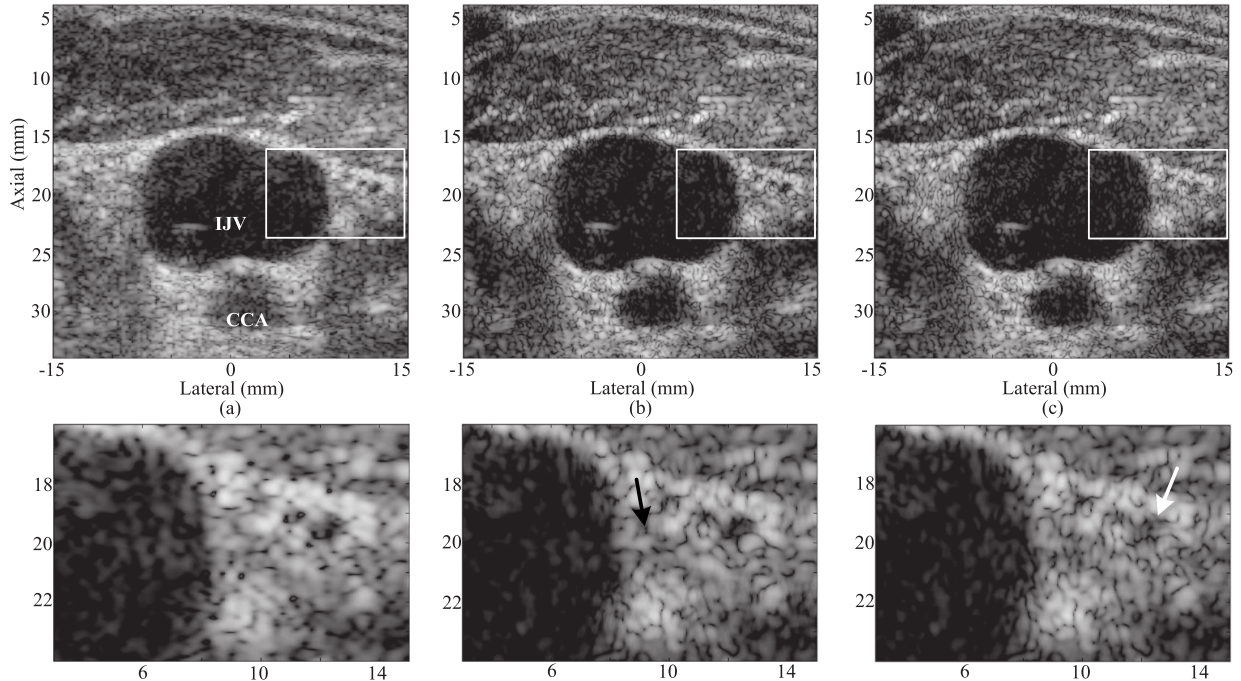

Fig. 8. Top: B-mode image of the IJV and CCA in transverse view. Both are surrounded by the thyroid gland. The images are generated and displayed using (a) dynamic focusing, (b) unified PB beamforming, and (c) coherent PB beamforming. Labels in (a) are also relevant to the corresponding regions in the images in (b) and (c). The images in (b) and (c) are generated with data from 32 transmits. Bottom: magnified views of the regions enclosed by the white rectangles in the top images. All images are log-compressed and displayed with a dynamic range of 50 dB.

At this lower center frequency, the broader speckle sizes at the focal depth in the unified PB images are shown clearly in Fig. 7(b) and (d), especially in the magnified views. Similar metrics to those in Table II, but measured on these images, are calculated and summarized in Table III.

E. In Vivo Study

We acquired ultrasound imaging data from an ultrasound carotid experiment with a 53-year-old volunteer using the ULA-OP system. The experiment was conducted with appropriate ethical clearance and informed consent. The image generated with conventional dynamic focusing is shown in Fig. 8(a). It is a cross-sectional view of the internal jugular vein (IJV), the common carotid artery (CCA), and surrounding structures. These vessels carry the oxygen-rich blood cells up to the brain and down to the heart. In the image, the IJV and the CCA are displayed as anechoic regions, resulting in deeper structures appearing to have higher echogenicity (enhancement).

We applied the unified and coherent PB beamformers to the prebeamformed data and show the results in Fig. 8(b) and (c). Both have much higher resolution than dynamic focusing, which is consistent with the results observed in our simulation

and phantom studies. Improvements in the contrast can be seen clearly in the region of the CCA in the images generated by PB algorithms. To show the difference between the unified and coherent PB beamformers, we have magnified a portion of each image including the IJV boundaries around 20 mm [enclosed by the white rectangles in Fig. 8(a)–(c)]. On the magnified view of Fig. 8(b), there is blurring on the region at the focal depth from the unified PB (indicated with the black arrow), while the surrounding tissue is displayed with a finer speckle pattern in the corresponding region of the coherent PB image. We measure the coherence length of the speckle in these regions. The metric with the unified PB is around 0.58 mm, while that measured with the coherent PB is approximately 0.43 mm. In Fig. 8(c), there are three small patches of reduced scattering in the coherent PB image that are less visible than those in the unified PB image (the biggest one is indicated by the white arrow). It is unclear whether these are small blood vessels or artifacts in the generated images. This, however, may indicate a loss of contrast, which is in agreement with the higher sidelobes of the coherent PB approach, shown in the point target simulation. The imaging results overall show that the improvements of the coherent PB over the unified PB in resolution are preserved in an *in vivo* context.

IV. CONCLUSION

In this paper, we have extended our pressure field analysis and propose the coherent PB beamformer as a new higher resolution approach to the computation of ultrasound B-scan images. Similar to the unified PB, the coherent PB is also designed to accumulate the data associated with the highest energy pulses. When neither pulse dominates the waveshape, however, it picks data associated with both pulses and combines them with appropriate phase matching. The coherent PB algorithm has been demonstrated using simulations and experimental and *in vivo* data. It shows improvements in spatial resolution over the unified PB approach around the focal depth and makes it optimal over the entire imaging region.

The coherent PB beamformer was developed in parallel with the minimum-variance-based beamformer in [13]. They are based on similar frameworks of field pattern analysis. Compared with the minimum-variance algorithm, the coherent PB approach may have lower spatial and contrast resolution for scattering fields that comply with certain statistical restrictions. However, the coherent PB is a faster and more robust method and can work on any type of scatterer field. Like the unified PB, the coherent PB collects signals based on a time delay calculation. This limits the coherent PB to the use of one or two data points in each received waveform. Improvements offered by the beamformer, therefore, are limited to the lateral resolution. The axial resolution could be improved if some deconvolution could be incorporated into the beamformer to reduce the temporal correlation in the received waveforms. This motivates our future work.

ACKNOWLEDGMENT

REFERENCES

[1] J. S. Hwang and T. K. Song, "A study of the display pixel-based focusing method in ultrasound imaging," *Ultrason. Imag.*, vol. 23, no. 1, pp. 1–18, 2001.

[2] Y. Lee, W. Y. Lee, C. E. Lim, J. H. Chang, T. K. Song, and Y. Yoo, "Compounded direct pixel beamforming for medical ultrasound imaging," *IEEE Trans. Ultrason., Ferroelect., Freq. Control*, vol. 59, no. 3, pp. 573–582, Mar. 2012.

[3] J. A. Jensen et al., "Ultrasound research scanner for real-time synthetic aperture data acquisition," *IEEE Trans. Ultrason., Ferroelect., Freq. Control*, vol. 52, no. 5, pp. 881–891, May 2005.

[4] J. A. Jensen, S. I. Nikolov, K. L. Gammelmark, and M. H. Pedersen, "Synthetic aperture ultrasound imaging," *Ultrasonic*, vol. 44, pp. e5–e15, Dec. 2006.

[5] R. E. Daigle, "Ultrasound imaging system with pixel oriented processing," U.S. Patent 2009/0 112 095 A1, May 19, 2009.

[6] M.-H. Bae and M.-K. Jeong, "A study of synthetic-aperture imaging with virtual source elements in B-mode ultrasound imaging systems," *IEEE Trans. Ultrason., Ferroelect., Freq. Control*, vol. 47, no. 6, pp. 1510–1519, Nov. 2000.

[7] C. Pass and H. Ermert, "A 100-MHz ultrasound imaging system for dermatologic and ophthalmologic diagnostics," *IEEE Trans. Ultrason., Ferroelect., Freq. Control*, vol. 43, no. 4, pp. 545–551, Jul. 1996.

[8] C. H. Frazer and W. D. O'Brien, Jr., "Synthetic aperture techniques with a virtual source element," *IEEE Trans. Ultrason., Ferroelect., Freq. Control*, vol. 45, no. 1, pp. 196–206, Jan. 1998.

[9] R. Zemp and M. F. Insana, "Imaging with unfocused regions of focused ultrasound beams," *J. Acoust. Soc. Amer.*, vol. 121, no. 3, pp. 1491–1498, 2007.

[10] H. Andresen, S. I. Nikolov, and J. A. Jensen, "Precise time-of-flight calculation for 3-D synthetic aperture focusing," *IEEE Trans. Ultrason., Ferroelect., Freq. Control*, vol. 56, no. 9, pp. 1880–1887, Sep. 2009.

[11] C. Kim et al., "Evaluation of ultrasound synthetic aperture imaging using bidirectional pixel-based focusing: Preliminary phantom and *in vivo* breast study," *IEEE Trans. Biomed. Eng.*, vol. 60, no. 10, pp. 2716–2724, Oct. 2013.

[12] N. Q. Nguyen and R. W. Prager, "High-resolution ultrasound imaging with unified pixel-based beamforming," *IEEE Trans. Med. Imag.*, vol. 35, no. 1, pp. 98–108, Jan. 2016.

[13] N. Q. Nguyen and R. W. Prager, "Minimum variance approaches to ultrasound pixel-based beamforming," *IEEE Trans. Med. Imag.*, vol. 36, no. 2, pp. 374–384, Feb. 2017.

[14] J. A. Jensen and N. B. Svendsen, "Calculation of pressure fields from arbitrarily shaped, apodized, and excited ultrasound transducers," *IEEE Trans. Ultrason., Ferroelect., Freq. Control*, vol. 39, no. 2, pp. 262–267, Mar. 1992.

[15] J. A. Jensen, "FIELD: A program for simulating ultrasound systems," in *Proc. IEEE 10th Nordic-Baltic Conf. Biomed. Imag.*, vol. 34. Mar. 1996, pp. 351–353.

[16] P. Tortoli, L. Bassi, A. Dallai, F. Guidi, and S. Ricci, "ULA-OP: An advanced open platform for ultrasound research," *IEEE Trans. Ultrason., Ferroelect., Freq. Control*, vol. 56, no. 10, pp. 2207–2216, Oct. 2009.

[17] R. S. C. Cobbold, *Foundations of Biomedical Ultrasound*. New York, NY, USA: Oxford Univ. Press, 2007.

[18] K. Mustafe, P.-C. Li, and M. O'Donnell, "Synthetic aperture imaging for small scale systems," *IEEE Trans. Ultrason., Ferroelect., Freq. Control*, vol. 42, no. 3, pp. 429–442, May 1995.

[19] R. F. Wagner, S. W. Smith, J. M. Sandrik, and H. Lopez, "Statistics of speckle in ultrasound B-scans," *IEEE Trans. Sonics Ultrason.*, vol. 30, no. 3, pp. 156–163, May 1983.

[20] S. W. Smith, R. F. Wagner, J. M. Sandrik, and H. Lopez, "Low contrast detectability and contrast/detail analysis in medical ultrasound," *IEEE Trans. Sonics Ultrason.*, vol. 30, no. 3, pp. 164–173, May 1983.

[21] S. Mehdizadeh, A. Austeng, T. F. Johansen, and S. Holm, "Eigenspace based minimum variance beamforming applied to ultrasound imaging of acoustically hard tissues," *IEEE Trans. Med. Imag.*, vol. 31, no. 10, pp. 1912–1921, Oct. 2012.

[22] M. F. Insana, T. J. Hall, and L. T. Cook, "Backscatter coefficient estimation using array transducers," *IEEE Trans. Ultrason., Ferroelect., Freq. Control*, vol. 41, no. 5, pp. 714–723, Sep. 1994.
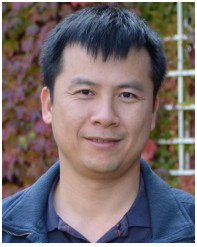
Nghia Q. Nguyen received the Ph.D. degree in electrical and computer engineering from the University of Illinois at Urbana-Champaign, Champaign, IL, USA, in 2012. His dissertation topic was objective assessment of ultrasound image quality.

He was a Post-Doctoral Research Associate with the Los Alamos National Laboratory, Los Alamos, NM, USA, from 2012 to 2014, where he developed ray-tracing methods for ultrasound tomography. Since 2014, he has been a Senior Research Associate in Information Engineering with the University of Cambridge, Cambridge, U.K. His current research interests include medical image analysis, ultrasound beamforming, image processing, inverse problem, and ultrasound tomography.

Richard W. Prager received the Ph.D. degree in information engineering from the University of Cambridge, Cambridge, U.K., in 1987.

He was head of teaching at Cambridge University Engineering Department from 2006 to 2012. He is currently Professor of Engineering and since 2014 has been Head of Cambridge University School of Technology. He founded the Medical Imaging Group in the Cambridge Engineering Department, Cambridge, UK, in 1992. He is one of the principal architects of the both the Stradx and Stradwin freehand 3-D ultrasound systems. Significant projects have included fast and accurate calibration systems for tracked 3-D ultrasound, real-time 3-D ultrasound deconvolution for image enhancement, and a hybrid scanner that combines the benefits of both tracked and mechanically swept 3-D ultrasound.

Prof. Prager is a Fellow of Queens' College Cambridge and of the Institution of Engineering and Technology. He is a Chartered Engineer (CEng).